

## A three-dimensional microgeodynamic model of melt geometry in the Earth's deep interior

Jesse Wimert<sup>1</sup> and Saswata Hier-Majumder<sup>1,2</sup>

Received 9 November 2011; revised 27 February 2012; accepted 28 February 2012; published 11 April 2012.

[1] This article presents a three-dimensional microgeodynamic model of grain-melt geometry in partially molten rocks. The isotropic unit cell of the partially molten rock is characterized by a face-centered-cubic symmetry, consisting of rhombic dodecahedral grains. The variation of surface tension between grain-grain and grain-melt contacts excites a coupled viscous flow within grains and the interstitial melt, leading to a steady state grain-melt geometry. We obtain the fractional area of intergranular contact, contiguity, from these models as a function of melt volume fraction, between melt fractions of 0.05 and 0.25. Comparison with previous results indicates that the contiguity in three-dimensional models is lower than in two-dimensional models. The contrast between two- and three-dimensional values of contiguity increases at high melt volume fractions. We apply our model to the ultralow-velocity zones (ULVZs) and the very low velocity province (VLVP) in the Earth's core-mantle boundary. The observed seismic signature of the ULVZ and VLVP can be explained by peridotite melt volume fractions between 0.08 and 0.12 and between 0.01 and 0.05, respectively, in a matrix of elastic properties similar to the Preliminary Earth Reference Model.

**Citation:** Wimert, J., and S. Hier-Majumder (2012), A three-dimensional microgeodynamic model of melt geometry in the Earth's deep interior, *J. Geophys. Res.*, 117, B04203, doi:10.1029/2011JB009012.

### 1. Introduction

[2] Melt volume fraction in partially molten rocks influences the effective physical properties of the rock [Walsh, 1969; Watt *et al.*, 1976; Takei, 1998, 2000, 2002; Yoshino *et al.*, 2005; Scott and Kohlstedt, 2006; ten Grotenhuis *et al.*, 2005; Faul, 2001; Hier-Majumder, 2008; Hier-Majumder and Abbott, 2010; Hustoft and Kohlstedt, 2006]. As the volume fraction of melt in grain edge tubules and pockets increases, the fractional area of intergranular contact, contiguity, decreases. Since the elastic strength of the load-bearing framework is controlled by contiguity, the effective bulk and shear moduli of partially molten rocks decrease with an increase in melt fraction. As the melt fraction reaches the threshold of disaggregation, intergranular contact is lost, and the effective shear modulus becomes zero [Takei, 2002]. Thus, the velocity of shear waves is more sensitive to partial melting than that of *P* waves. In interpreting the melt volume fraction from observed differential reductions in seismic body wave velocities, a parametrization of the contiguity-melt fraction relation is thus necessary.

[3] The relation between contiguity and melt fraction has been studied in a number of theoretical and experimental studies. The seminal work of von Barga and Waff [1986]

explored the influence of melt fraction and dihedral angle on the three-dimensional geometry of melt tubules and pockets for melt volume fractions up to 0.05. Experimental results, obtained from high-resolution micrographs of polished sections of synthetic and natural rocks, investigate the relation between melt fraction and contiguity over a larger range of melt fraction and various dihedral angles (see Yoshino *et al.* [2005] for a compilation of data). Recently, X-ray microtomography has revealed direct visualization of three-dimensional melt distribution in partially molten aggregates [Zhu *et al.*, 2011; Watson and Roberts, 2011]. Contiguity, however, is yet to be measured directly using this technique. Currently, the only measurement of contiguity at moderate to high melt fractions arise from two-dimensional measurements or extrapolation of the three-dimensional model of von Barga and Waff [1986].

[4] This work investigates the melt microstructure and the variation of contiguity with melt fraction at melt fractions between 0.05 and 0.25. Following a recent suite of works [Hier-Majumder, 2008, 2011; Hier-Majumder and Abbott, 2010], we employ a set of coupled mass and momentum conservation equations aided with appropriate boundary and jump conditions (balance equations for change in traction across the grain-melt interface) for a partially molten rock. Variation of surface tension between grain-grain and grain-melt contacts drives a viscous flow in the interior of the grains and the melt tubules until a steady state is attained. We consider a face-centered-cubic (FCC) unit cell containing a melt volume fraction of approximately 0.26 and composed of spherical grains as the unperturbed, reference state. As the perturbation arising from interaction with the neighboring

<sup>1</sup>Department of Geology, University of Maryland, College Park, Maryland, USA.

<sup>2</sup>Center for Scientific Computation and Applied Mathematical Modeling, University of Maryland, College Park, Maryland, USA.

grains increases, the contact faces become more faceted, bringing the centers of the grains together, and reducing the volume of the unit cell. Once the contiguity and melt volume fraction are calculated from the steady state grain shape, we use the “equilibrium geometry” model of *Takei* [2002] to obtain the effective bulk and shear moduli of the unit cell.

[5] Two kinds of space-filling polyhedra are used to describe the grain shape in dense, multiparticle aggregates [*Lissant*, 1966; *German*, 1985; *Park and Yoon*, 1985; *von Bargen and Waff*, 1986]. While *von Bargen and Waff* [1986] employed a truncated octahedral or tetrakaidecahedral geometry, *Park and Yoon* [1985] argued that a rhombic dodecahedron geometry is equally applicable for sintering models of multiphase materials. *Lissant* [1966] argues that tetrakaidecahedral geometry is preferred for melt fractions below 0.06, and that the geometry of the rhombic dodecahedron is preferred for higher melt fractions. Later work of *Takei* [1998] also argues in favor of the rhombic dodecahedron geometry. This work explores the contiguity-melt fraction relation beyond the narrow range between 0 and 0.05 studied by *von Bargen and Waff* [1986]. In addition, the equilibrium geometry model of *Takei* [2002] used to process the output of this model is ideally suited for rhombic dodecahedral grains. Therefore, we selected rhombic dodecahedral symmetry to describe perturbed grains.

[6] Earth’s core-mantle boundary presents two relevant test cases for this study. First, an L-shaped, very low velocity province (VLVP) located at the core-mantle boundary beneath the South Atlantic and Indian oceans, is marked by reduction of shear wave velocity by 2% to 12% [*Wen et al.*, 2001; *Wen*, 2001; *Wang and Wen*, 2004]. The *P* wave velocity in this region is also reduced by up to 3%. The approximately 300 km high VLVP has an areal extent of  $1.8 \times 10^7$  km<sup>2</sup> [*Wang and Wen*, 2004]. The shear wave velocity drop associated with the VLVP is too large to explain by thermal anomaly [*Wen et al.*, 2001]. In addition, the VLVP is spatially correlated with the geochemical DUPAL anomaly [*Wen*, 2006]. Combination of these observations indicate that the VLVP likely contains partial melt, possibly distributed in an inhomogeneous manner, as evident from a vertical gradient of the shear wave velocity reduction [*Wen et al.*, 2001; *Wen*, 2001; *Wang and Wen*, 2004].

[7] Secondly, a patchwork of thin, dense, low-viscosity zones, termed ultralow-velocity zones (ULVZ) has been observed on the mantle side of the Earth’s core-mantle boundary [*Rost et al.*, 2005; *Williams and Garnero*, 1996; *Wen and Helmberger*, 1998; *Hutko et al.*, 2009; *Rost and Revenaugh*, 2003; *McNamara et al.*, 2010; *Thorne and Garnero*, 2004]. Where present, these structures are typically associated with large reduction of both *S* (25%–30%) and *P* (8%–10%) wave velocities. Typically, the seismic signature of the ULVZ has been explained by partial melting [*Williams and Garnero*, 1996]. Results from laboratory experiments, however, postulate that iron-rich high-pressure phases can also explain some of the observed velocity reductions [*Wicks et al.*, 2010; *Mao et al.*, 2006].

[8] Explaining the seismic signature of the ULVZ by only iron-rich solids, however, is difficult to reconcile with a few other seismic and experimental observations. Occurrence of ULVZ beyond the stability field of iron-rich postperovskite [*Garnero and McNamara*, 2008] indicates that such ULVZ

occurrences must be explained by other phenomena. Strong iron depletion in magnesiowüstite in contact with outer core liquid [*Ozawa et al.*, 2008, 2009] implies that Mg<sub>0.16</sub>Fe<sub>0.84</sub>O is not a stable composition for parts of ULVZ that might be in direct contact with the outer core. High-pressure melting experiments on fertile peridotites also indicate that ferropericlase and Ca-rich perovskite are likely to be molten and in equilibrium with solid Mg perovskite under core-mantle boundary conditions [*Fiquet et al.*, 2010]. These experimental results and numerical models [*Stixrude and Karki*, 2005; *Stixrude et al.*, 2009] indicate that the silicate solidus temperature at the core-mantle boundary is likely lower than the geotherm. Partial melting in the ULVZ likely leads to an iron-rich silicate melt hosted in a silicate matrix [*Nomura et al.*, 2011].

[9] If partially molten, dynamic processes operative within the ULVZ depend strongly on the extent of melting. A relatively large volume fraction of dense melt is difficult to retain uniformly distributed within the rocky matrix [*Hernlund and Tackley*, 2007], as the high-density melt will tend to pool near the bottom. *Hernlund and Jellinek* [2010] suggested stirring of the mushy ULVZ can prevent such a gravitational drainage. *Hier-Majumder et al.* [2006] suggest that capillary tension at grain-grain contact can reduce the drainage efficiency of the melt in a macroscopic scale. In a microscopic scale, matrix deformation arising from stirring of the ULVZ can enhance melt segregation by grain boundary wetting [*Hier-Majumder et al.*, 2004; *Hier-Majumder*, 2011]. Dissolution-precipitation-driven healing, however, can rehomogenize melt out of some grain boundary films, reducing the gravitational drainage efficiency [*Takei and Hier-Majumder*, 2009; *King et al.*, 2011]. Finally, vertical distribution of melt within the ULVZ can be reflected in the vertical gradients of *S* and *P* wave velocities within the ULVZ [*Rost et al.*, 2006]. Inferring the extent of melting from the seismic signature of the ULVZ is thus crucial in understanding the internal dynamics of these structure.

[10] This article is organized in the following manner: We present the governing equations for grain-melt geometry, solution techniques, and the averaging scheme for the unit cell in section 2. The results for grain-melt shape, relationship between contiguity and melt fraction, and comparison with previous studies is presented in section 3. Finally, we discuss the limitations of our model, the role of melt composition, seismic signature of two- and three-dimensional models, and the implications for melting in the VLVP and the ULVZ in section 4.

## 2. Methods

[11] The semianalytical technique in this work models the melt volume fraction, contiguity, and elastic properties averaged over a unit cell, consisting of 14 grains arranged in a FCC symmetry. Each grain in the unit cell is contiguous to 12 other grains, while the interstitial volume is saturated with melt. The surface tension on each grain varies spatially between grain-grain and grain-melt contacts. The spatial gradient of surface tension excites a flow within the grains and the interstitial melt. When the forces arising from pressure, surface tension, and viscous deformation balance each other, the steady state geometry is attained. Once the steady state shape of each individual grain is derived from the

governing equation, we populate the unit cell with identical grains to calculate the melt volume fraction and contiguity.

[12] To systematically study the variation of contiguity with melt volume fraction, we consider a reference unit cell. In this reference unit cell, each grain, described by a unit sphere, makes only point contacts with its neighbors. In this configuration, contiguity is zero, and the volume fraction of the interstitial space is approximately 0.26, the porosity of FCC packed spheres. In partially molten rocks, this melt fraction, termed the “disaggregation melt fraction,” or the “rheologically critical melt fraction,” is marked by a sharp reduction in viscosity [Scott and Kohlstedt, 2006]. Next, we consider the influence of neighboring grains on each grain, via surface tension, as a perturbation to this reference state. As the perturbation increases, the grains become more faceted, increasing the area of intergranular contact. Due to faceting, it is possible to pack the grains into a smaller unit cell, reducing the volume fraction of interstitial space. We carried out a series of numerical experiments with different extents of perturbation in each experiment. We then measured the melt fraction and contiguity in each experiment. Finally, we fit the contiguity-melt fraction data to obtain a relation between contiguity and melt volume fraction. This section outlines the steps involved in this process.

[13] This work does not incorporate anisotropic grain boundary energy and the influence of varying dihedral angle on contiguity. We also assume that the physical properties of each grain in the unit cell are identical, rendering the unit cell monomineralic. We discuss the influence of anisotropy, deformation, and different mineral and melt compositions on inferred seismic signatures in section 4.1.

## 2.1. Governing Equations

[14] Consider a collection of grains in a partially molten unit cell. We express the steady state shape of each grain as a small perturbation from a sphere. The shape function  $F_k$  describing the  $k$ th grain is given by,

$$F_k = r - a(1 + \epsilon f_k) = 0, \quad (1)$$

where  $f_k$  is an unknown function, and the coefficient of deformation,  $\epsilon$ , is a constant. The variable  $r$  is the radial distance from the center of the grain. We notice that the unit normal to the grain,  $\hat{\mathbf{n}}_k$ , is given by Leal [1992],

$$\hat{\mathbf{n}}_k = \frac{\nabla F_k}{|\nabla F_k|} = \hat{\mathbf{r}} - \epsilon \nabla f_k. \quad (2)$$

where  $\hat{\mathbf{r}}$  is the unit radial vector.

[15] In the reference state or zeroth order, velocities within each grain and the melt phase are considered zero. The pressure within each phase, however, has a nonzero zeroth-order component. Within the  $k$ th grain ( $i = k$ ) or melt ( $i = m$ ), total dynamic pressure  $p_i^{total}$ , total velocity  $\mathbf{u}_i^{total}$ , and stress tensors  $\mathbb{T}_i^{total}$  are given by,

$$\mathbf{u}_i^{total} = \epsilon \mathbf{u}_i, \quad (3)$$

$$p_i^{total} = p_i^0 + \epsilon p_i, \quad (4)$$

$$\mathbb{T}_i^{total} = -p_i^{total} \mathbf{I} + \epsilon \mu_i (\nabla \mathbf{u}_i + \nabla \mathbf{u}_i^T), \quad (5)$$

where  $\mu_i$  is the viscosity and  $\mathbf{I}$  is the identity matrix.

[16] In the perturbed state, the coupled flow within each grain and the melt are governed by the conservation of mass and momentum within each particle and the melt. Each particle and the melt are treated as incompressible viscous fluids, leading to the first-order equations,

$$0 = \mu_i \nabla^2 \mathbf{u}_i - \nabla p_i, \quad (6)$$

and

$$0 = \nabla \cdot \mathbf{u}_i. \quad (7)$$

[17] To solve for the unknown velocities, pressures, and shape functions, we need to impose two sets of boundary conditions. First, the velocity is assumed to be continuous at the interface of the  $k$ th particle, implying no-slip at this interface,

$$\mathbf{u}_k|_{F_k=0} = \mathbf{u}_m|_{F_k=0}. \quad (8)$$

Next, the continuity of traction across the interface  $F_k = 0$  requires [Leal, 1992, chapter 5],

$$\Delta \mathbb{T}^k \cdot \hat{\mathbf{n}}^k + \tilde{\nabla} \gamma - \gamma \hat{\mathbf{n}}^k (\nabla \cdot \hat{\mathbf{n}}^k) = 0, \quad (9)$$

where  $\Delta \mathbb{T}^k$  is the stress drop on the surface of the  $k$ th grain and  $\gamma$  is the interfacial tension. The surface gradient operator  $\tilde{\nabla}$  is defined as [Manga and Stone, 1995]

$$\tilde{\nabla} = [1 - \hat{\mathbf{n}}^k \hat{\mathbf{n}}^k] \cdot \nabla, \quad (10)$$

where  $\hat{\mathbf{n}}^k$  is the unit normal vector and  $\nabla$  is the gradient operator. The first term in the left hand side of the stress jump condition, equation (9), is the differential traction across the interface, the second term arises from the variation of interfacial tension on a grain, and the third term arises from curvature driven surface tension force. The normal component of the stress jump condition is termed the Laplace condition while the tangential component is termed as the Marangoni condition [Hier-Majumder, 2008; Leal, 1992]. The total surface tension  $\gamma$  can also be expressed as a sum of the reference surface tension  $\gamma_0$  and a perturbation surface tension  $\gamma_1$ ,

$$\gamma = \gamma_0 + \epsilon \gamma_1. \quad (11)$$

The perturbation  $\gamma_1$  arises from the alteration of the surface properties due to contact with other grains. The nature of this function depends on the packing geometry of the grains and is discussed in section 2.3. Finally, the evolution of the shape of the  $k$ th grain is governed by the kinematic relation [Leal, 1992],

$$\frac{\partial F_k}{\partial t} + \mathbf{u}_k \cdot \nabla F_k = 0. \quad (12)$$

[18] Taken together, conservation equations (6) and (7), the no-slip boundary condition (8), normal component of the stress jump condition (9), and the kinematic condition (12) can be used to solve for the first-order unknown velocity  $\mathbf{u}_i$ , pressure  $p_i$ , and shape perturbation of the  $k$ th particle  $f_k$ . First, analytical solutions to the velocity and pressure fields are obtained using the technique of solid harmonics.

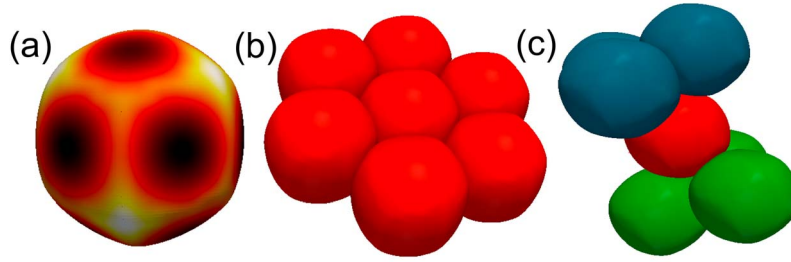


**Figure 1.** Packing arrangement of the grains. (a) An individual grain, with the areas of contact with other grains in dark color. (b) The central grain in red is contiguous to 12 other grains, 6 along the  $\theta = \pi/2$  plane (also shown in red), (c) 3 above at  $\theta = \sin^{-1}(\sqrt{1/3})$  (shown in blue), and 3 below at an angle of  $\theta = \pi - \sin^{-1}(\sqrt{1/3})$  (shown in green).

Details of this technique are provided in Appendix A. Once the velocity and pressure fields are obtained, those solutions are substituted into the normal component of the stress jump condition (9) to obtain a second-order partial differential equation in the unknown shape perturbation  $f_k$ . The above equations were nondimensionalized by using,

$$p_i = \frac{\mu_i u_0}{a} p'_i, \quad (13)$$

$$\mathbf{u}_i = u_0 \mathbf{u}'_i \quad (14)$$

$$\mathbf{r} = a \mathbf{r}' \quad (15)$$

$$\gamma = \gamma_0 \gamma', \quad (16)$$

where  $u_0$  is a reference velocity,  $a$  is the grain size, and  $\gamma_0$  is a reference value of grain-melt surface tension. The nondimensional conservation equations, after dropping the primes, are given by

$$0 = \nabla^2 \mathbf{u}_i - \nabla p_i, \quad (17)$$

and

$$0 = \nabla \cdot \mathbf{u}_i. \quad (18)$$

By analytically solving equations (17) and (18), as explained in Appendix A, we obtain the governing equation for the perturbed shape function  $f_k$ , in the steady state,

$$\nabla^2 f_k = \frac{2}{\gamma_0} \gamma_1, \quad (19)$$

where  $\gamma_0$  is a constant. As evidenced by equation (19), in the steady state, only perturbation in the surface tension controls the perturbed grain shape.

## 2.2. Packing Arrangement

[19] In the rhombic dodecahedron geometry, each grain has a coordination number of 12. The grain is surrounded by six other grains in its equatorial plane and three grains, offset from each other, each on the layer above and below the equatorial layer, leading to an A-B-C packing arrangement. The diagram in Figure 1 outlines the coordination symmetry

of a rhombic dodecahedral grain. This packing arrangement is used in the next section to prescribe the surface tension distribution of each grain.

## 2.3. Prescription of Surface Tension

[20] Following the prescription of *Takei* [1998], we identify 12 contact patches on each rhombic dodecahedral grain, where the perturbed surface tension is equal to  $\gamma'_{gg}$ , the grain-grain surface tension, and is equal to  $\gamma'_{gm}$  everywhere else:

$$\gamma_1(\theta, \phi) = \left( \gamma'_{gg} - \gamma'_{gm} \right) \sum_{i=1}^{12} h_i(\theta) g_i(\phi) \quad (20)$$

where  $h_i(\theta)$  and  $g_i(\phi)$  are combinations of step functions in  $\theta$  and  $\phi$ , the colatitude and the azimuthal angle in spherical coordinates, respectively. The difference in the two values of surface tension is used for the perturbation surface tension since  $\gamma_1$  is being added to the reference value of surface tension. The step functions are used to model contact patches on the grain surface. This allows for equation (20) to be separated into its  $\theta$  and  $\phi$  components. Multiple step functions are used for each contact face to create the shape of a rhombus [*Wimert*, 2011].

[21] To solve the partial differential equation in (19), we expand both  $f$  and  $\gamma_1$  in a series of spherical harmonic functions,  $Y_l^m(\theta, \phi)$  as

$$f_k = \sum_{m=0}^{\infty} \sum_{l=-m}^m f_{l,m} Y_l^m(\theta, \phi) \quad (21)$$

and

$$\gamma_1 = \sum_{m=0}^{\infty} \sum_{l=-m}^m \gamma_{l,m} Y_l^m(\theta, \phi). \quad (22)$$

Applying the numerical prescription for  $\gamma_1$  in equation (20) and using the orthonormality condition of spherical harmonics, we get the following equation for the coefficients  $\gamma_{l,m}$

$$\gamma_{l,m} = \left( \gamma'_{gg} - \gamma'_{gm} \right) \sum_{i=1}^{12} \int_{\theta} \int_{\phi} [h_i(\theta) g_i(\phi) Y_l^{m*}(\theta, \phi)] \sin \theta \, d\theta \, d\phi, \quad (23)$$

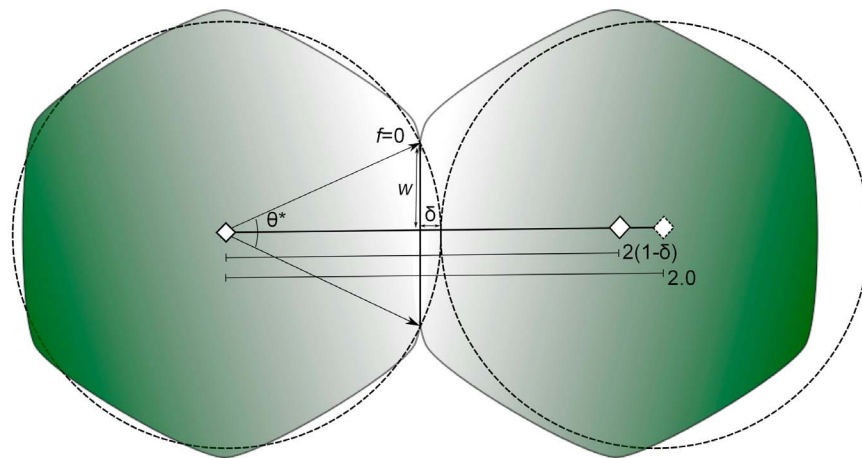


**Figure 2.** A cross section in the  $x$ - $y$  plane, displaying the relationship between the radius of the contact face and the decrease in distance between grain centers due to flattening. By measuring  $\theta^*$ , the value of  $\delta$  and  $w$  are found using equations (25) and (26), respectively.

where the asterisk denotes complex conjugation. Taking the spherical harmonic transform of equation (19), the coefficients in the expansion of  $f$  and  $\gamma_1$  are related by,

$$f_{l,m} = -\frac{2}{\gamma_0 l(l+1)} \gamma_{l,m}. \quad (24)$$

Since  $h_l(\theta)$  and  $g_l(\phi)$  are known, the coefficients  $\gamma_{l,m}$  can be calculated from (23), which we then insert into equation (24) to obtain the coefficients in the expansion of the perturbed shape function  $f_k$ . Finally, combining equations (1) and (21), we obtain the perturbed shape of the  $k$ th grain.

#### 2.4. Calculation of Melt Volume Fraction and Contiguity

[22] The melt volume fraction for the model was calculated from the geometry of the unit cell. As explained in section 2.2, each grain is surrounded by six grains in the equatorial plane ( $\theta = \pi/2$ ), three grains above, and three grains below the equatorial plane. Each layer of grains above and below the equatorial plane are offset from each other, leading to a FCC packing symmetry. If each grain was a perfect, unit sphere, similar to the unperturbed state, cell parameters  $a$ ,  $b$ , and  $c$  of this unit cell would be equal to  $2\sqrt{2}$ . Assuming the empty space between the grains is saturated by melt, the melt volume fraction in this case would be 0.26.

[23] We calculated the area of nearly circular grain-grain contact by measuring the radius of the contact. The radius,  $w$ , and the shortening  $\delta$ , displayed in Figure 2, vary linearly with the magnitude of the perturbation coefficient  $\epsilon$ ,

$$\delta = \epsilon \left( 1 - \cos \frac{\theta^*}{2} \right), \quad (25)$$

$$w = \epsilon \sin \frac{\theta^*}{2}, \quad (26)$$

where  $\theta^*$  is the angle subtended by an arc of contact in the cross section displayed in Figure 2. In the absence of perturbation ( $\epsilon = 0$ ) both  $w$  and  $\delta$  are zero, rendering zero

contiguity at the disaggregation melt fraction. From the numerical solution of varying  $f_k$  on the surface of the  $k$ th particle, the boundary of this circle is marked by the contour of  $f_k = 0$ , the line of zero perturbation.

[24] If the radius of the unperturbed sphere is shortened by an amount  $\delta$  at the center of a contact face, then the distance between the centers of two unit spheres is reduced to  $2(1 - \delta)$ . Knowing the location of the centers of the touching, flattened grains, we calculate the volume of the unit cell. Next, we calculate the volume of each grain numerically by using the software Paraview. The total volume of solids in each FCC unit cell is equal to 4 times the volume of one individual grain ( $8 \times \frac{1}{8}$  corner grains +  $6 \times \frac{1}{2}$  face centered grains = 4 grains). Thus, the melt fraction is calculated assuming the void within the unit cell is completely saturated by melt.

[25] In successive numerical experiments, we varied the parameter  $\epsilon$  between 0.1 and 1. For each of the runs, we set the nondimensional surface tension parameters,  $\gamma'_{gm} = 0.1$  and  $\gamma'_{gg} = 0.5$ . We carried out a total of 20 numerical experiments. In all simulations, the magnitude of the maximum perturbation to the shape, was always  $O(10^{-2})$ . These maximum values of perturbations were associated with flattened intergranular contacts and bulged melt-grain contacts. The small values of perturbation justify the underlying linear analysis, in which term  $O(\epsilon^2)$  or higher were neglected. The data on contiguity and melt fraction from these experiments were then fit with a polynomial function to obtain a melt fraction-contiguity relation between melt fractions of 0 and the disaggregation melt fraction.

[26] Once the numerical solution for the perturbed shape functions are obtained, we calculated contiguity,  $\psi$ , of the faceted grain as the sum of area fraction of the 12 contact patches,

$$\psi = \frac{1}{4\pi} \sum_{i=1}^{12} A_i, \quad (27)$$

where  $A_i$  is the area of an individual patch.

**Table 1.** Constants Used in Vinet Equation of State to Calculate the Bulk Modulus of Melt<sup>a</sup>

	Midocean Ridge Basalt	Peridotite Melt	MgSiO <sub>3</sub> Melt <sup>b</sup>	Mg <sub>2</sub> SiO <sub>4</sub> Melt <sup>c</sup>
$K_0$ (GPa)	18.1 <sup>d</sup>	24.9 <sup>d</sup>	10.1	115.0
	15.5 <sup>e</sup>	16.5 <sup>e</sup>		
$K'_0$	5.5 <sup>d</sup>	6.4 <sup>d</sup>	7.6	2.9
	7.2 <sup>e</sup>	7.2 <sup>e</sup>		
$P$ (GPa)	135.99 <sup>d</sup>	136.84 <sup>d</sup>	135.99	136.04
	136.17 <sup>e</sup>	136.46 <sup>e</sup>		
$K$ (GPa)	452.98 <sup>d</sup>	555.28 <sup>d</sup>	574.99	421.79
	577.21 <sup>e</sup>	583.44 <sup>e</sup>		
$\rho/\rho_0$	2.40 <sup>d</sup>	2.03 <sup>d</sup>	2.28	1.74
	2.13 <sup>e</sup>	2.10 <sup>e</sup>		

<sup>a</sup>The values of  $P$  and  $K$  were obtained using the constants from the first two rows corresponding to the values of  $\rho/\rho_0$  reported in the last row.

<sup>b</sup>Stixrude and Karki [2005].

<sup>c</sup>Mosenfelder et al. [2007].

<sup>d</sup>Ohtani and Maeda [2001].

<sup>e</sup>Guillot and Sator [2007].

## 2.5. Calculation of Seismic Velocities

[27] Once the contiguity and melt fraction for each experiment was determined, we used the equilibrium geometry model of Takei [2002] to calculate the effective elastic moduli and seismic velocities of the partially molten aggregate. In addition to the contiguity and melt volume fraction, bulk moduli of the solid and the melt, shear modulus and poisson's ratio in the solid, and the ratio of density between the solid and the liquid is required. For the solid phase, these parameters were provided from the Preliminary Reference Earth Model (PREM) at the core-mantle boundary condition. We also assumed that the density of the melt is equal to that of the solid under this condition [Stixrude and Karki, 2005; Mosenfelder et al., 2007].

[28] We calculated the bulk modulus of melt from the Vinet Equation Of State (EOS), relating pressure  $P$  to density  $\rho$  by the implicit relation [Poirier, 2000, section 4.5.2],

$$P = 3K_0 \left( \frac{\rho}{\rho_0} \right)^{\frac{2}{3}} \left[ 1 - \left( \frac{\rho}{\rho_0} \right)^{-\frac{1}{3}} \right] \exp \left( \frac{3}{2} (K'_0 - 1) \left[ 1 - \left( \frac{\rho}{\rho_0} \right)^{-\frac{1}{3}} \right] \right), \quad (28)$$

where  $K_0$  is the bulk modulus,  $\rho_0$  is the density, and  $K'_0 = dK/dP$  is the pressure derivative of the bulk modulus at  $P = 0$ . The bulk modulus at pressure  $P$  is obtained from the EOS, by using the relation

$$K = \left( \frac{\rho}{\rho_0} \right) \frac{dP}{d \left( \frac{\rho}{\rho_0} \right)}. \quad (29)$$

To test the influence of different melt compositions, we calculated the melt bulk modulus for midocean ridge basalt (MORB) [Ohtani and Maeda, 2001; Guillot and Sator, 2007], peridotite [Ohtani and Maeda, 2001; Guillot and Sator, 2007], MgSiO<sub>3</sub> [Stixrude and Karki, 2005], and Mg<sub>2</sub>SiO<sub>4</sub> [Mosenfelder et al., 2007] melts. The values of relevant constants and calculated values of pressure  $P$ , melt density ratio  $\rho/\rho_0$ , and melt bulk modulus  $K$  are presented in Table 1. We tested the effect of melt composition via melt

bulk modulus on the seismic properties for fixed melt fractions of 0.08, 0.1, and 0.12, respectively. Finally, we used a bulk modulus of 555.28 GPa corresponding to that of a peridotitic melt of Ohtani and Maeda [2001] to calculate the seismic signature as a function of melt volume fraction.

## 3. Results

[29] This section outlines the model results. First, we discuss the solution to the shape perturbation function. Next, the results for the melt volume fraction and contiguity in a unit cell are discussed. Finally, we compare the melt fraction-contiguity relation from our results with the results of three-dimensional numerical simulation from von Bagen and Waff [1986], two-dimensional model of Hier-Majumder et al. [2006], and experimental measurements of Yoshino et al. [2005].

### 3.1. Solutions for Grain Shape and Melt Geometry

[30] The surface of a single grain, colored by the magnitude of the perturbed shape function  $\epsilon f$ , is visualized in Figure 3. Dark values indicate regions of flattening. Bright, bulging patches represent contact with three different kinds of melt units. Tubules are linear grain-melt contacts, located between two dark intergranular contacts. Pockets are situated between four contiguous dark intergranular contacts and at the intersection of four tubules. Finally, three tubules meet each other at junctions, which are situated at the intersection of three grain-grain contact patches. In this geometry, each grain has a total of 6 pockets, 8 junctions, and 24 tubules along the 24 edges of the rhombic dodecahedron.

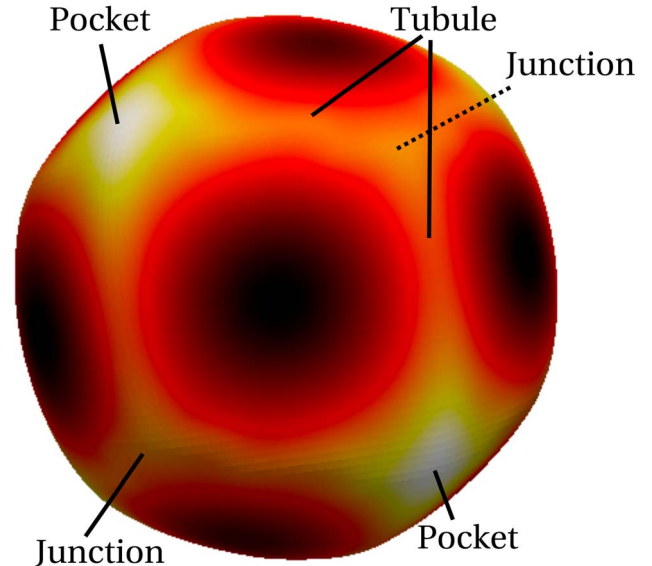


**Figure 3.** Shape of a single grain, calculated from equation (19) and colored by the value of  $\epsilon f$ . A positive  $f$  value (yellow and white) perturbs the initial sphere by pushing out, while a negative  $f$  value (red and black) deforms the sphere by pushing in and flattening the grain surface. The color scale is the same as given in Figure 4. Contacts with melt pockets, tubules, and junctions are marked on the grain.

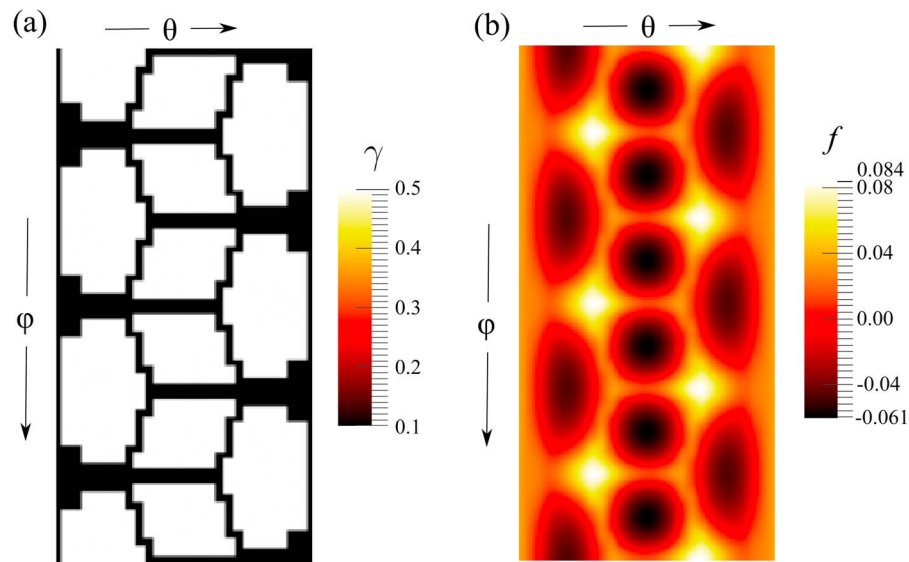


**Figure 4.** Surface map of (a) the prescribed surface tension and (b) perturbed shape of the grain. The two surface maps are related by equations (19) and (24). Higher values of surface tension correspond to negative values of  $\epsilon f$  and perturb the initial sphere by flattening the grain surface, while lower values of surface tension correspond to positive values of  $\epsilon f$  and deform the sphere by pushing out the grain surface (see Figure 3).

[31] Surface tension forces perturbation of the grain shape. The color map in Figure 4 depicts the prescribed surface tension and the resulting perturbation of the reference shape in the  $\theta - \phi$  space. The accompanying colorbars indicate the magnitude of the perturbation to both the prescribed surface tension and the shape. Since the prescribed surface tension assumes only two values, the color on Figure 4a is binary. As indicated by the surface plot in Figure 3, negative relief corresponds to regions of flattening. Tension on the intergranular contact flexes the grain surface inward while slight bulges are produced at the grain-melt contact. It can also be seen from Figures 3 and 4 that the contact patches given by the shape function  $f$  are more circular compared to the rhombus shaped patches of surface tension prescribed by equation (20). These contact patches are similar to the direct prescription of the patch geometry by *Takei* [1998].

[32] Figure 5 shows melt tubules, junctions, and pockets that form around an individual grain for systems with different melt volume fractions. The melt volume fraction increases from Figure 5a to Figure 5d from 0.06 to 0.22. For clarity, two junctions and pockets are identified on Figure 5a. The visualizations illustrate that as the melt volume fraction increases, the melt tubules and pockets grow larger, and the area of the circular grain-grain contacts decreases. The contiguity in the visualizations decrease from 0.38 in Figure 5a to 0.02 in Figure 5d. The values of melt volume fractions and contiguity for all numerical experiments are described in Table 2.

[33] We also compare the change in shapes of grains and tubules as the melt volume fraction increases, in Figure 6, depicting a melt tubule along with three grains. In this set of visualizations, produced from the same simulations as in Figure 5, melt volume fraction increases from 0.06 to 0.22. The color map on the surface of the grains represent the

magnitude of the perturbed shape function. Two features of the microstructure become clear as the melt volume fraction increases. First, the area of tubule cross section increases with an increase in melt volume fraction. Second, the grains

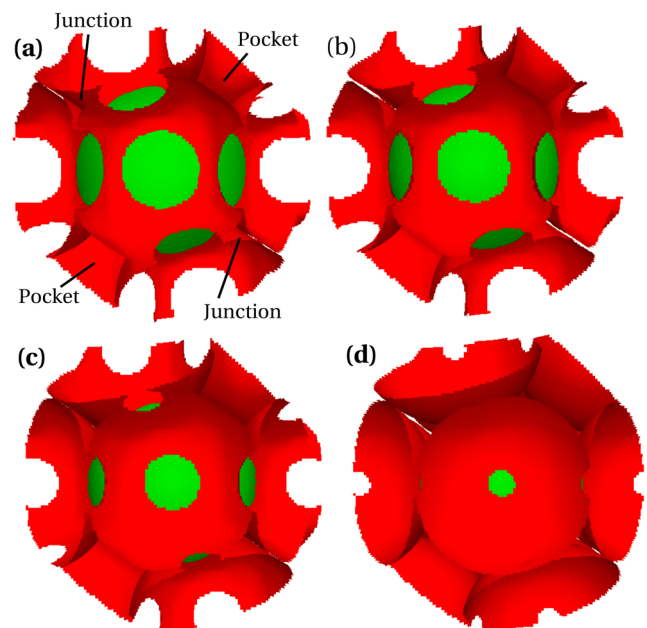


**Figure 5.** Melt tubules and pockets surrounding an individual grain for four different melt fractions. Red coloring represents grain-melt contact, and green coloring represents grain-grain contact. The melt volume fractions for the given configurations are (a)  $\phi = 0.06$ , (b)  $\phi = 0.11$ , (c)  $\phi = 0.14$ , and (d)  $\phi = 0.22$ .

**Table 2.** Contiguity and Melt Fraction Measurements<sup>a</sup>

$\epsilon$	Melt Volume %	Contiguity
1.000	5.45 ± 0.27	0.418 ± 0.009
0.953	6.58 ± 0.24	0.379 ± 0.007
0.905	7.69 ± 0.21	0.342 ± 0.006
0.858	8.79 ± 0.18	0.307 ± 0.005
0.811	9.86 ± 0.16	0.274 ± 0.004
0.763	10.92 ± 0.13	0.243 ± 0.003
0.716	11.97 ± 0.11	0.214 ± 0.002
0.668	12.99 ± 0.09	0.187 ± 0.002
0.621	14.01 ± 0.07	0.161 ± 0.001
0.574	15.01 ± 0.06	0.137 ± 0.001
0.526	15.99 ± 0.04	0.116 ± 0.001
0.479	16.95 ± 0.03	0.096 ± 0.001
0.432	17.91 ± 0.02	0.078 ± 0.000
0.384	18.84 ± 0.01	0.062 ± 0.000
0.337	19.77 ± 0.00	0.047 ± 0.000
0.289	20.68 ± 0.18	0.035 ± 0.000
0.242	21.57 ± 0.02	0.024 ± 0.000
0.195	22.46 ± 0.02	0.016 ± 0.000
0.147	23.33 ± 0.03	0.009 ± 0.000
0.100	24.18 ± 0.03	0.004 ± 0.000

<sup>a</sup>The errors are associated with the variations in the numerical estimates of the grain volume and area of grain-grain contact patches [Wimert, 2011].

become less faceted and more round shaped. The color map on the grain surface, corresponding to the shape perturbation, becomes even as the melt fraction increases.

### 3.2. Melt Fraction and Contiguity in the Unit Cell

[34] In the perturbed state, the unit cell of the rhombic dodecahedron is substantially smaller when compared to an FCC packed unit cell of spheres. The surface plots in Figure 7 visualizes a unit cell from two different orientations. In Figure 7a blue arrows indicate the unit cell vectors in the FCC lattice. For a unit sphere, all three lattice parameters are equal to a uniform value of 2.82. In the perturbed state, the distance between the centers of the contiguous grains is reduced. In the case depicted in Figure 7, each unit cell vector is reduced to a length of 2.61, indicating an approximately 7.4% shortening in each direction. Such a shortening leads to a denser packing of the unit cell. The volume of the cell depicted in Figure 7 is 17.78, about 27% smaller than a unit cell produced by touching spheres, whose volume is 22.43. While the volume of each grain is about 4.19, the volume of a unit sphere. Since the volumes of the grains remain nearly unchanged, flattening at intergranular contacts reduces the available interstitial space. The volume fraction of interstitial melt is 0.05, substantially smaller than the interstitial melt volume fraction of 0.26 in the reference unit cell.

[35] Both the melt volume fraction and contiguity varied with a variation in  $\epsilon$ . Figure 8 illustrates the relationships between  $\epsilon$  and melt volume fraction and contiguity. Melt volume fraction varies nearly linearly with  $\epsilon$ , while contiguity varies with  $\epsilon$  in a nonlinear manner.

[36] The data on contiguity and melt fraction from our numerical experiments are fitted with a fifth-order polynomial of the form

$$\psi = p_1\phi^5 + p_2\phi^4 + p_3\phi^3 + p_4\phi^2 + p_5\phi + p_6. \quad (30)$$

To ensure that contiguity tends to unity at zero melt volume fraction, we fixed  $p_6 = 1$  in equation (30). The coefficients

obtained from the fitting function are given in Table 3. Measures for the goodness of the fit, sum of squared errors and  $R^2$  are given by  $1.67 \times 10^{-4}$  and 0.9995, respectively.

### 3.3. Comparison With Previous Studies

[37] The contiguity-melt fraction relation from our work can be compared with previous experimental and numerical data. The plot in Figure 9 compares our results and the fit to our data to the results from the model of *von Bargen and Waff* [1986] for a dihedral angle of  $\sim 30^\circ$ . Also overlaid on the plot are contiguity measurements from synthetic midocean ridge basalt (MORB) and olivine bearing aggregate and a fertile spinel lherzolite rock from Killbourne Hole, New Mexico by *Yoshino et al.* [2005]. Notice that the formula for solid-solid surface area in equation (8) of *von Bargen and Waff* [1986] needs to be corrected by adding a constant approximately equal to  $\pi$ , such that the plot of their equation (8) matches their Figure 7. In the article, their equation (8) erroneously indicates that the area of grain-grain contact decreases to zero at zero melt fractions. The results of *von Bargen and Waff* [1986] are only applicable for small melt fractions (less than 0.05 melt volume fraction) but the fit of the results are extrapolated with a dotted line for higher melt fractions in the plot.

[38] In the same plot, our fit is extrapolated to zero melt fraction with a broken curve. As the curves indicate, between melt volume fractions of 0 and 0.02, our fit predicts a contiguity slightly lower than that of *von Bargen and Waff* [1986]. Between melt volume fractions of 0.02 and 0.12, our model predicts a slightly higher value of contiguity than *von Bargen and Waff* [1986]. Finally, our model predicts that

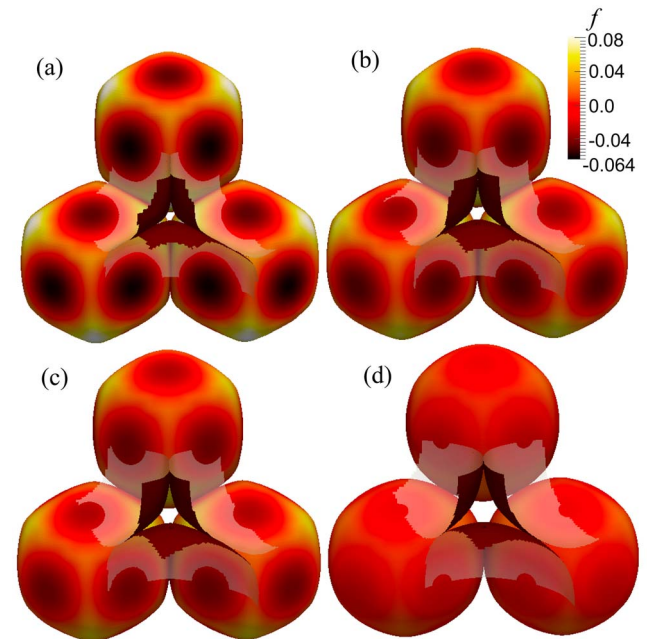


**Figure 6.** Melt tubule and three grains for four different melt fractions. The color scale represents the value of  $\epsilon f$ , the perturbation in shape function. As the melt volume fraction increases, the channel grows larger, and the area of grain-grain contact decreases. The melt fractions for the given configurations are (a)  $\phi = 0.06$ , (b)  $\phi = 0.11$ , (c)  $\phi = 0.14$ , and (d)  $\phi = 0.22$ .

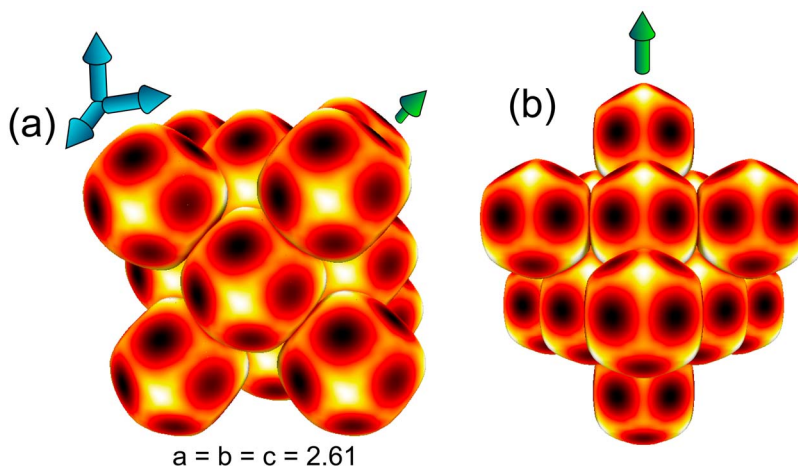


**Figure 7.** A calculated multiparticle unit cell with a face-centered-cubic (FCC) geometry. The dimension of the unit cell parameters  $a$ ,  $b$ , and  $c$  is equal to 2.61, approximately 7.4% shorter than an FCC packed with solid spheres, for which  $a = b = c = 2.82$ . The volume of the unit cell is 17.72, while the volume of each grain is 4.19, leading to a melt volume fraction of 0.05. (a) The FCC unit cell with blue arrows indicating the edges of the cubic unit cell. The green arrow points in the direction of the normal to each close-packed plane. (b) A view of the unit cell along the close-packed planes.

contiguity becomes zero at a disaggregation melt fraction of 0.26, while *von Bargen and Waff* [1986] predicts a disaggregation melt fraction of 0.19. Our slightly higher estimate of the disaggregation melt fraction agrees better with the results of *Scott and Kohlstedt* [2006], who report a rheological transition coincident with loss of contiguity, that takes place between melt volume fractions of 0.25 and 0.3. Overall, the results from our model and that of *von Bargen and Waff* [1986] are in good agreement. The similarity between these two models become clearer when compared with two-dimensional models and measurements. Both our data and that of *von Bargen and Waff* [1986] predict a contiguity lower than the measurements of *Yoshino et al.* [2005]

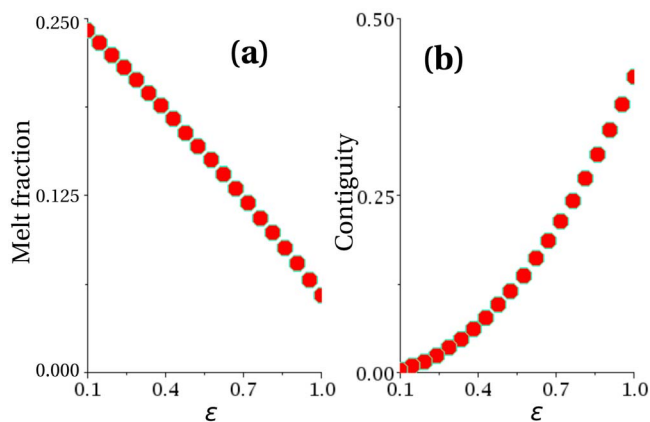


**Figure 8.** Plots showing the effect  $\epsilon$  has on (a) melt volume fraction and (b) contiguity. Increasing  $\epsilon$  results in greater grain-grain contact area and a denser packing arrangement. Notice how the relationship between  $\epsilon$  and melt volume fraction is nearly linear, while the relationship between  $\epsilon$  and contiguity is nonlinear.

and the geometric model of *Hier-Majumder et al.* [2006]. The contrast increases further at higher melt fractions.

[39] The discrepancy between the two-dimensional measurements and models and three-dimensional numerical models primarily arises from the fact that two-dimensional sections can underestimate the grain-melt contact area and melt volume fraction. *Hier-Majumder and Abbott* [2010] demonstrate that in a cubic grain with cylindrical tubules along edges, a two-dimensional cross section underestimates the volume fraction of melt by a factor of 3. The area of melt-grain contact is underestimated by a factor of 6 in two dimensions. As a result, when the two-dimensional data from their model was corrected to three dimensions, the contiguity decreased. Such corrections were not applied to the two-dimensional geometric model of *Hier-Majumder et al.* [2006] or the experimental measurements of *Yoshino et al.* [2005, section 2.3].

[40] Natural and synthetic samples in the study of *Yoshino et al.* [2005] display variations in grain size, surface tensions, and mineral compositions, while both two- and three-dimensional models of *Hier-Majumder et al.* [2006], *von Bargen and Waff* [1986], and the current work assume monomineralic and isotropic unit cells filled with uniform-sized grains. Despite these differences, the two-dimensional model of *Hier-Majumder et al.* [2006] and the experimental

**Table 3.** Parameters for Fit to the Contiguity ( $\psi$ ) as a Function of Melt Fraction ( $\phi$ )<sup>a</sup>

$p_1$	$p_2$	$p_3$	$p_4$	$p_5$	$p_6$
-8065.00	6149.00	-1778.00	249.00	-19.77	1.00
-9844.00	5022.00	-2033.00	224.50	-20.59	0.00
-6287.00	7275.00	-1522.00	273.50	-18.94	0.00

<sup>a</sup>The fit is given by  $\psi = p_1\phi^5 + p_2\phi^4 + p_3\phi^3 + p_4\phi^2 + p_5\phi + p_6$ . The entries in the second and third rows indicate the error bounds to the parameters within 95% confidence bound. For the fit the values of the sum of squared errors and  $R^2$  are  $1.67 \times 10^{-4}$  and 0.9995, respectively.

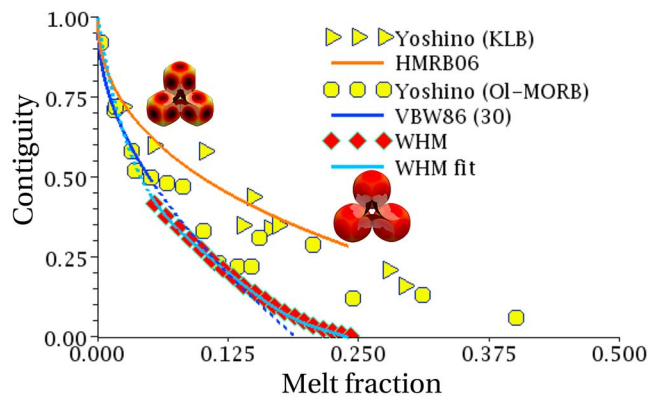


**Figure 9.** Comparison between contiguity from this work, the results of *von Bargen and Waff* [1986], the experimental measurements of *Yoshino et al.* [2005], and the two-dimensional model of *Hier-Majumder et al.* [2006]. The results of *von Bargen and Waff* [1986] are limited to melt volume fractions below 0.05, but the fit is continued to higher melt fractions (dashed blue line). Extrapolation of the fit to our data is also plotted (dotted light blue line). The circular data points and the triangular data points indicate measurements by *Yoshino et al.* [2005] of olivine-mid-ocean ridge basalt (Ol-MORB) and KLB, respectively. The orange and dark blue curves represent the contiguity-melt fraction relationships determined by the study of *Hier-Majumder et al.* [2006] and *von Bargen and Waff* [1986], respectively. The red data points are results found in this study. The plot shows that two-dimensional models, and experimental measurements dependent on two-dimensional slices, result in higher values of contiguity than three-dimensional models.

measurements of *Yoshino et al.* [2005] uniformly overestimate contiguity compared to the three-dimensional models. We conclude that overestimation of contiguity in two dimensions—rather than mineral chemistry, grain size distribution, and surface tension variations—exert a stronger control on the melt fraction contiguity relation.

#### 4. Discussion

[41] The result from this work bears a number of broader implications for melting in the Earth's deep interior. Using our contiguity-melt fraction data, we demonstrate that the seismic signature of the ULVZ at the core-mantle boundary can be explained by a smaller extent of melting than a two-dimensional microstructure would predict. We also provide an estimate of melt volume fraction for the VLVP beneath the South Atlantic and the Indian ocean. These topics are discussed in this section.

##### 4.1. Influence of Grain-Scale Variations

[42] In this section, we discuss the likely roles played by crystal anisotropy, deformation, mineral composition, and bimodal grain size distribution on the melt geometry.

[43] Similar to other poroelastic models [*Walsh*, 1969; *Watt et al.*, 1976; *Takei*, 1998; *Mavko et al.*, 2003], our calculations assume that the monomineralic unit cell is filled with isotropic crystals of equal grain size. In addition, we do

not consider the role of an applied external stress on melt segregation. Both crystal anisotropy and deformation lead to preferential wetting or dewetting of grain-grain contacts. *Takei* [2005] reports that dynamic wetting of grain boundaries and melt film formation due to an applied stress led to a drop in shear wave velocity in an anisotropic manner. While out of the scope of this present article, our semianalytical method can be extended in future studies to address the issue of crystal anisotropy. The underlying assumption of small perturbations in this work, however, breaks down in the presence of a large applied stress. Future studies on the role of deformation in redistribution of melt microstructure, will need to involve numerical solutions using the Boundary Elements Method (BEM) [*Hier-Majumder*, 2008; *Hier-Majumder and Abbott*, 2010].

[44] In addition, distribution of different mineral grains in multiminerale rocks can lead to asymmetric melt tubules. For example, *Zhu and Hirth* [2003] discuss the variations in the effective dihedral angle due to the variations in the composition of surrounding grains of olivine and orthopyroxene. Permeability of the partially molten aggregate, however, was practically insensitive to such variations in melt tubule symmetry above melt volume fractions of 0.04. According to the calculations of *Zhu and Hirth* [2003], the effect of varying mineral composition is likely insignificant within the range of melt volume fractions investigated in our study.

[45] Bimodal grain size can influence the spatial distribution of melt under a hydrostatic condition of stress. Owing to the high surface to volume ratio, *Wark and Watson* [2000] argue, pockets of small grain size can drain melt out of adjacent pockets of large grains by capillary tension. Such a redistribution can lead to spatial variation of melt fraction, and contiguity. If spatial distribution of pockets of differing grain size is statistically random, then the isotropic unit cell approximation is appropriate. In contrary, deformation can lead to recrystallization of grains and impart a fabric to the grain size distribution. Under such circumstances, our assumption of a uniform unit cell is inappropriate. This analysis, therefore, applies to partially molten aggregates free of deformation fabric or anisotropy.

##### 4.2. Influence of Melt Composition

[46] Melt composition influences the seismic signature of a partially molten aggregate in two ways. First, the bulk modulus of the melt, for a given volume fraction, varies with the melt composition. Second, melts of different compositions wet grain-grain contacts differently. In this section, we discuss these two issues in context of our prediction of melt volume fraction in the core-mantle boundary.

[47] The effective bulk modulus and the resulting drop in  $P$  wave velocities, depend both on the volume fraction and the composition of the melt. For realistic melt compositions, considered in this study, the former exerts a stronger influence on seismic signature than the latter. The data in Table 4 list the relative drop in  $P$  wave velocity for melts of MORB, peridotite,  $Mg_2SiO_4$ , and  $MgSiO_3$  compositions, for melt volume fractions of 0.08, 0.1, and 0.12, respectively. Bulk modulus of these melts, at core-mantle boundary pressure, are listed in Table 1. The shear wave velocity drop is independent of the bulk modulus of the melts. For the three melt volume fractions of 0.08, 0.1, and 0.12 listed in Table 4,

**Table 4.** Comparison of  $P$  Wave Velocity Reduction ( $\Delta V_p/V_p^0$ ) for Various Melt Compositions<sup>a</sup>

Melt Fraction	Midocean Ridge Basalt	Peridotite Melt	MgSiO <sub>3</sub> Melt <sup>b</sup>	Mg <sub>2</sub> SiO <sub>4</sub> Melt <sup>c</sup>
0.08	0.92 <sup>d</sup> 0.93 <sup>e</sup>	0.92 <sup>d</sup> 0.93 <sup>e</sup>	0.93	0.92
0.1	0.90 <sup>d</sup> 0.91 <sup>e</sup>	0.91 <sup>d</sup> 0.91 <sup>e</sup>	0.91	0.90
0.12	0.89 <sup>d</sup> 0.90 <sup>e</sup>	0.90 <sup>d</sup> 0.90 <sup>e</sup>	0.90	0.88

<sup>a</sup>Bulk moduli of the melts are reported in Table 1.

<sup>b</sup>Stixrude and Karki [2005].

<sup>c</sup>Mosenfelder et al. [2007].

<sup>d</sup>Ohtani and Maeda [2001].

<sup>e</sup>Guillot and Sator [2007].

$\Delta V_S/\Delta V_S^0$  values are 0.8, 0.76, and 0.71, respectively. For melt volume fractions of 0.08 and 0.1,  $\Delta V_p/\Delta V_p^0$  displays 1% compositional variability, which increases to 2% for a melt volume fraction of 0.12. The mean value of  $\Delta V_p/\Delta V_p^0$ , however, decreases by 3% with a 4% increase in the melt volume. If we neglect the seismic signature of the Mg end-member melts, peridotitic and MORB melts show 1% or less variation in  $\Delta V_p/\Delta V_p^0$ , at any given melt volume fraction. Thus, we conclude that melt volume fraction exerts a stronger control on the seismic signature than the melt compositions studied here.

[48] Small volume fractions of wetting melts mimic the seismic signature of high-volume fractions of less wetting melts. As a smaller area of intergranular contact is available to mechanically support the skeletal framework, the effective elastic moduli are comparatively low for wetting melts. For example, using the relations from *von Bargaen and Waff* [1986], for a melt volume fraction of 0.05, contiguity decreases from 0.56 to 0.46 by decreasing the dihedral angle from 60° to 20°. The same reduction in contiguity is achieved, using our contiguity-melt fraction relation, by increasing the melt volume fraction from 0.035 to 0.05. Thus, the influence of wetting behavior on contiguity is relatively modest, but not negligibly small. Future experimental work and numerical models will be helpful in quantifying this effect for three-dimensional microstructures.

### 4.3. Seismic Signature

[49] The contiguity of a partially molten rock, along with the melt volume fraction, strongly influences the effective elastic moduli. We discuss the reduction in elastic moduli and seismic velocities by melting for a solid whose physical properties are similar to the PREM model at the core-mantle boundary. All calculations presented in this section consider a peridotite melt composition, whose bulk modulus is determined by using the constants from *Ohtani and Maeda* [2001]. Figures 10a and 10b show the variation of the normalized shear and bulk modulus of the partially molten rock as a function of melt volume fraction and contiguity. As expected, only the normalized shear modulus displays a significant variation in Figure 10a. The response of the bulk modulus to melting, in general, and contiguity in specific, is caused by the more modest contrast between the bulk moduli of the solid and the melt compared to the contrast between their respective shear moduli. As the contiguity decreases, grain surfaces become more wet and the strength

of the skeletal framework decreases. This results in lower values of the shear modulus.

[50] Figure 10 also shows the variation of normalized  $S$  and  $P$  wave velocities as a function of melt volume fraction and contiguity. From the plot it can be seen that the  $S$  wave velocity is much more sensitive to changes in contiguity and melt volume fraction than are  $P$  waves. When increasing melt fraction from 0.10 to 0.20, the normalized  $S$  wave velocity is reduced from 0.75 to 0.40, while the normalized  $P$  wave velocity experiences a more modest reduction from 0.90 to 0.80.

[51] Our three-dimensional model predicts a sharper reduction in shear and  $P$  wave velocities compared to the two-dimensional, geometric model of *Hier-Majumder et al.* [2006]. The plots in Figure 11 compare the seismic velocity reduction between these two cases. The large variations between these two sets of models can lead to very different estimates on the degree of melting from observed shear and  $P$  wave velocity drops. For example, the observed shear and  $P$  wave velocity reductions between 0.70 to 0.75 and 0.90 to 0.92 in the ULVZ, can be explained by a range of melt volume fractions between 0.08 and 0.12 using the three-dimensional model. The two-dimensional model of *Hier-Majumder et al.* [2006] predicts similar velocity drops for much larger melt volume fractions. For example, a melt volume fraction as high as 0.23 can be used to explain the observed shear wave velocity reduction. As discussed earlier, the discrepancy between the two estimates arise from the overestimation of contiguity in the two-dimensional models.

### 4.4. Implications for VLVP and ULVZ

[52] The seismic velocities from our calculations can be used to constrain melting in the core-mantle boundary. The plot in Figure 12 compares shear and  $P$  wave velocity reductions as a function of melt volume fraction. Overlaid on the plot are the ranges of shear (25% to 30%) and  $P$  wave (8% to 10%) velocity reductions for the ULVZ and the range of shear wave velocity reduction (2% to 12%) for the VLVP. In the VLVP, the maximum  $P$  wave velocity reduction is 3%.

[53] The seismic velocity reduction in the VLVP can be explained by melt volume fractions of 0.01 to 0.05. This variation in melt volume fraction corresponds to the near linear decrease in shear wave velocity from the top to the bottom of the VLVP [*Wen et al.*, 2001; *Wen*, 2001; *Wang and Wen*, 2004]. In other words, our calculations indicate that the VLVP is marked by an increase in melt volume fraction from 0.01 near the top to 0.05 near the bottom. Such a vertical distribution of melt is consistent with capillary retention of dense melt in a viscous, rocky matrix [*Hier-Majumder et al.*, 2006]. At small to modest melt volume fractions, strong gradients of capillary tension prevent complete pooling of the dense melt into a thin layer at the bottom of the partially molten zone [*Hier-Majumder et al.*, 2006; *Hier-Majumder and Courtier*, 2011].

[54] In contrast to the modest melt volume fraction of the VLVP, the ULVZ is marked by a larger volume fraction of melt. As the plot in Figure 12 indicates, the range of the combined shear and  $P$  wave velocity signatures of the ULVZ can be matched by a melt volume fractions between 0.08 and 0.12. This estimate from our three-dimensional models are substantially lower than the estimate by *Williams and*

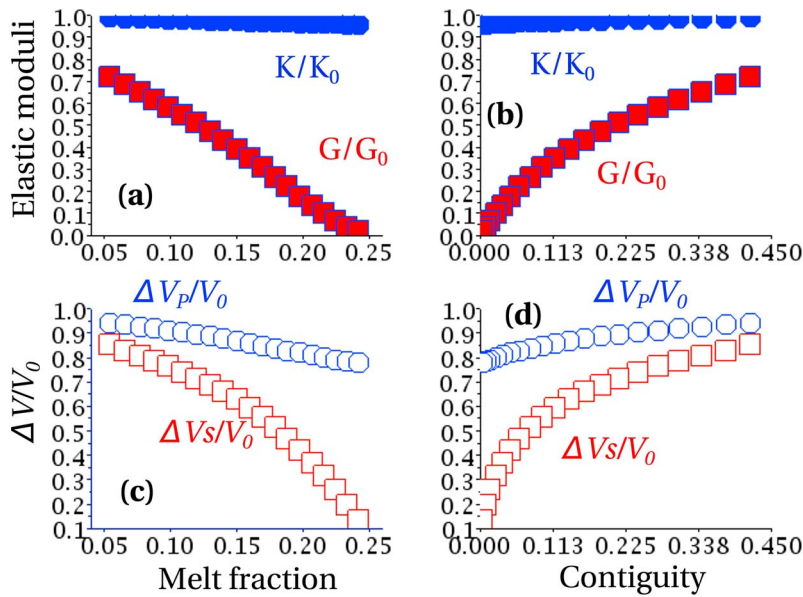


**Figure 10.** Plots of the changes in normalized shear and bulk modulus and the drop of seismic velocity of the partially molten rock as a function of melt volume fraction and contiguity. The ratio between the effective bulk ( $K$ ) and shear ( $G$ ) moduli and solid bulk ( $K_0$ ) and shear ( $G_0$ ) moduli in a partially molten aggregate as a function of (a) melt volume fraction and (b) contiguity. The ratio of seismic velocities of a partially molten rock to the seismic velocities in the absence of melting as a function of (c) melt volume fraction and (d) contiguity.

Garnero [1996], who, based on a melt inclusion model of poroelasticity, concluded that a melt volume fraction of up to 0.3 is required to explain the velocity reductions in the ULVZ, if the melt resides primarily in the tubules. As displayed in Figure 11, two-dimensional models of contiguity also predict a similarly high melt volume fraction based on the shear and  $P$  wave velocity reductions.

[55] One important consequence of the lesser amount of melting predicted by the three-dimensional model is the reduction of the effective viscosity of the ULVZ. Laboratory experiments on the stability of plumes [Jellinek and Manga,

2004] and a gravity current model of ULVZ spreading [Hier-Majumder and Revenaugh, 2010] predict that the ULVZ is likely two orders of magnitude weaker than the ambient mantle. The large degree of melting predicted by the two-dimensional model of contiguity, however, will reduce the effective viscosity to values much lower than these estimates.

[56] In a recent experimental study, Wicks *et al.* [2010] proposed that the differential drop in shear and  $P$  wave velocities similar to those in the ULVZ can be observed in an Fe-rich magnesiowüstite ( $Mg_{0.16}Fe_{0.84}O$ ) matrix. In a previous work, Mao *et al.* [2006] suggested that an Fe-rich

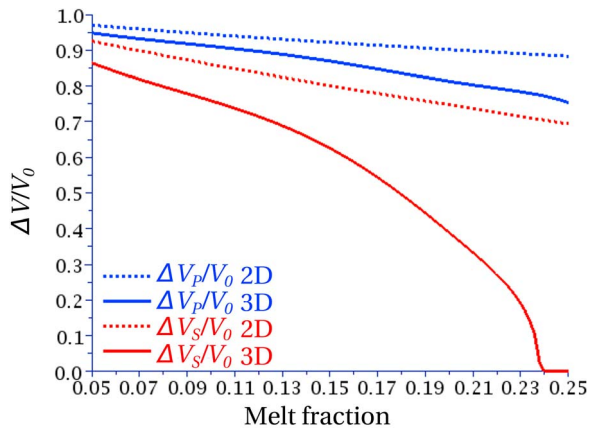


**Figure 11.** Ratio of seismic velocities of a partially molten rock to the seismic velocities in the absence of melting as a function of melt volume fraction. The seismic velocities from this study (solid lines) are compared to seismic velocities predicted by the two-dimensional study of Hier-Majumder *et al.* [2006] (dotted lines).

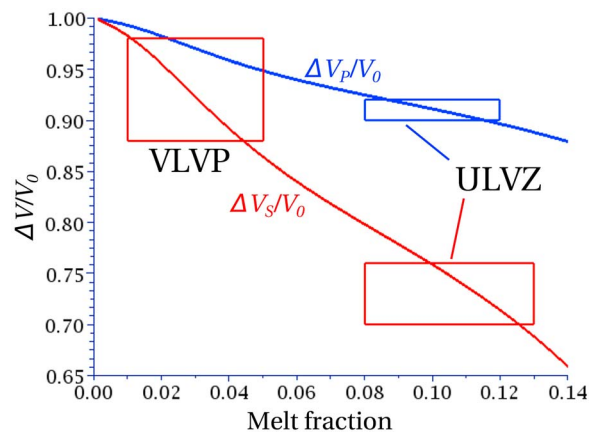


**Figure 12.** Fractional decrease in seismic wave velocities as a function of melt volume fraction. The red box marked “VLVP” indicates the range of shear wave velocity reduction in the VLVP. The two boxes marked “ULVZ” represent the  $P$  (blue) and shear (red) wave velocity reductions.

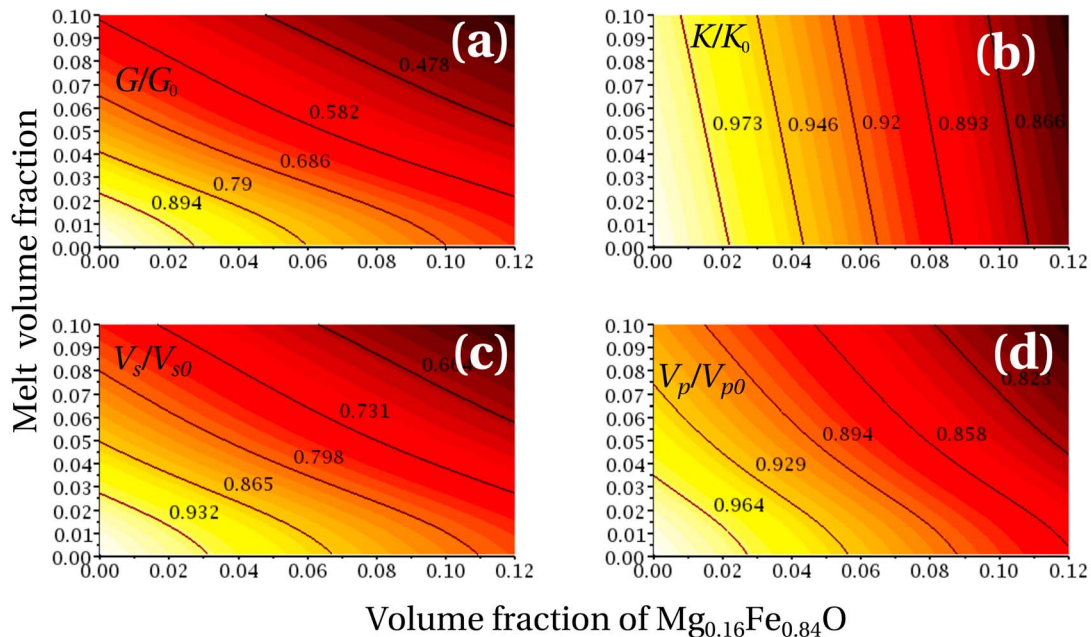


**Figure 13.** Map of seismic signature as a function of volume fraction of  $\text{Mg}_{0.16}\text{Fe}_{0.84}\text{O}$  and melt. Contour lines are overlaid on the color maps of (a) normalized shear modulus, (b) normalized bulk modulus, (c) normalized shear wave velocity, and (d) normalized  $P$  wave velocity.

postperovskite phase can also explain the observed reduction in bulk sound velocity within the ULVZ. Three lines of evidence suggest that only postperovskite or  $\text{Mg}_{0.16}\text{Fe}_{0.84}\text{O}$  falls short of explaining the seismic signature of the ULVZ. First, in a number of regions, the ULVZ has been detected beyond postperovskite stability field [Garnero and McNamara, 2008]. Second, a separate set of high-pressure experiments indicate that magnesiowüstite in contact with outer core liquid, will be strongly depleted in iron [Ozawa *et al.*, 2008], if not entirely consumed by outer core liquid [Ozawa *et al.*, 2009]. Finally, melting experiments on fertile peridotites [Fiquet *et al.*, 2010] indicate that ferropericlase is likely the first phase to melt under core-mantle boundary conditions, resulting in a ferropericlase and Ca perovskite melt in equilibrium with Mg perovskite. Recent experimental results from Nomura *et al.* [2011] report that a transition in the spin state of Fe likely leads to a dense, iron rich melts in the core-mantle boundary conditions.

[57] If a large volume fraction of  $\text{Mg}_{0.16}\text{Fe}_{0.84}\text{O}$  is somehow stabilized in the ULVZ, its seismic signature can trade off with the melt volume fraction. Using our contiguity-melt fraction relationship, we calculated the seismic velocity drops and effective bulk and shear moduli of the ULVZ, as a function of the melt volume fraction and  $\text{Mg}_{0.16}\text{Fe}_{0.84}\text{O}$  volume fraction in the solid. The color map in Figure 13 demonstrate the variations in normalized shear modulus, bulk modulus,  $S$  wave velocity, and  $P$  wave velocity variations as functions of volume fractions of  $\text{Mg}_{0.16}\text{Fe}_{0.84}\text{O}$  and melt. The effective bulk and shear moduli of the solids are calculated from the Reuss bound of  $S$  and  $P$  wave velocities and density of  $\text{Mg}_{0.16}\text{Fe}_{0.84}\text{O}$  and a solid of PREM composition. As suggested by Wicks *et al.* [2010], in the absence of melting, a volume fraction of 0.12 is required to explain the observed reductions in the shear and  $P$  wave velocities. If the solid composition is exactly similar to PREM, then

approximately 0.1 volume fraction of melt is necessary. The composition of ULVZ for a given reduction in  $S$  and  $P$  wave velocity drop can be explained by any points on the corresponding contour lines in Figures 13c and 13d. As the shape of the contours indicate, the composition can be explained by a near linear tie line between the melted and unmelted aggregates.

## 5. Conclusions

[58] We present a new three-dimensional, microgeodynamic model of contiguity in partially molten rocks. In our model, the FCC unit cell contains 14 rhombic dodecahedral grains. Our results extend the range of available contiguity-melt fraction model from a melt fraction of 0.05 to the disaggregation fraction of 0.26. For a given melt fraction, contiguity from our experiments is lower than the contiguity from two-dimensional models and data. Consequently, the three-dimensional model predicts a larger drop in seismic velocities for a given melt fraction than two-dimensional models. We also conclude that the variation in volume fraction of melt exerts a stronger influence on the seismic signature compared to varying the composition of the melt between MORB and peridotite. In a partially molten aggregate containing peridotite melt in a PREM solid, seismic signatures of the two compositional anomalies in the core mantle boundary—the VLVP and the ULVZ—can be explained by melt volume fractions between 0.01 to 0.05 and 0.08 to 0.12, respectively.

## Appendix A: Analytical Solution for Viscous Flow

[59] We build analytical solutions for the nondimensional velocity and pressure fields within each grain and the melt phase using vector solid harmonic functions [Leal, 1992,

chapter 4]. This technique is useful to construct solutions from a characteristic vector or tensorial quantity. First, we notice that the velocity of the melt phase,  $\mathbf{u}_m$  can be expressed as a function of dynamic pressure  $p_m$  and an unknown harmonic function  $\mathbf{v}_m$  ( $\nabla^2 \mathbf{v}_m = 0$ ), as

$$\mathbf{u}_m = \frac{1}{2} \mathbf{x} p_m + \mathbf{v}_m, \quad (\text{A1})$$

where  $\mathbf{x}$  is the position vector. Such a prescription of velocity guarantees that the nondimensional momentum conservation equation, (17), is automatically satisfied.

[60] The next step is to build the harmonic function  $\mathbf{v}_m$  from a characteristic vector  $\mathbf{d}$  relevant to the system. This vector should be constant, but, as we demonstrate, this vector does not appear in the steady state equation for shape function. One possible choice of this vector can be the displacement vector between the centers of two particles. Finally, we build the solution vector within the grain using growing harmonics (only positive powers of  $r$ , the distance from the center), while using decaying harmonics (negative powers of  $r$ ) to build the solution outside the grain. Notice that the nature of harmonics in this analysis is opposite to those in the work of *Hier-Majumder* [2011], as the origin was fixed within a melt pocket in that analysis.

[61] With these considerations in mind, we build the test solution for the harmonic functions  $\mathbf{v}_m$ ,  $\mathbf{v}_g$ ,  $p_m$ , and  $p_g$  as, (as

$$\mathbf{v}_m = \alpha_1 \left( \frac{\mathbf{x}(\mathbf{d} \cdot \mathbf{x})}{r^5} - \frac{\mathbf{d}}{3r^3} \right) + \beta_1 \frac{\mathbf{d}}{r} \quad (\text{A2})$$

$$p_m = c_1 \frac{\mathbf{x} \cdot \mathbf{d}}{r^3} \quad (\text{A3})$$

$$\mathbf{v}_g = \alpha_2 (\mathbf{x}(\mathbf{d} \cdot \mathbf{x}) - r^2 \mathbf{d}), \quad (\text{A4})$$

$$p_g = c_2 \mathbf{d} \cdot \mathbf{x}, \quad (\text{A5})$$

where  $\alpha_1$ ,  $\beta_1$ ,  $c_1$ ,  $\alpha_2$ , and  $c_2$  are unknown constant coefficients. We use mass conservation equation for both phases, the normal, and tangential components of the no-slip boundary condition to obtain the relations,

$$\alpha_1 = \frac{9\alpha_2}{8} \quad (\text{A6})$$

$$\beta_1 = -\frac{5\alpha_2}{8} \quad (\text{A7})$$

$$c_1 = -\frac{5\alpha_2}{4} \quad (\text{A8})$$

and

$$c_2 = -\alpha_2. \quad (\text{A9})$$

Finally, we substitute the melt velocity from equation (A1) at  $r = 1$ , into the nondimensional kinematic condition in the steady state to eliminate  $\alpha_2$  and obtain,

$$\nabla^2 F = \frac{2\gamma_1}{\gamma_0}. \quad (\text{A10})$$

[62] **Acknowledgments.** This research was made possible by the NSF grants EAR 0809689 and EAR 0911094. Insightful comments from L. Montési, W. Zhu, and S. Penniston-Dorland are greatly appreciated. David Bercovici provided a number of helpful comments in the early stages of the formulation. Constructive suggestions from the Associate Editor and two anonymous reviewers led to the incorporation of VLVP calculations and different melt compositions in the paper.

## References

- Faul, U. H. (2001), Melt retention and segregation beneath mid-ocean ridges, *Nature*, *410*, 920–923.
- Fiquet, G., A. L. Auzende, J. Siebert, A. Corgne, H. Bureau, H. Ozawa, and G. Garbarino (2010), Melting of peridotite to 140 gigapascals, *Science*, *329*(5998), 1516–1518.
- Garnero, E., and A. K. McNamara (2008), Structure and dynamics of Earth's lower mantle, *Science*, *320*(5876), 626–628.
- German, R. (1985), *Liquid Phase Sintering*, 240 pp., Plenum, New York.
- Guillot, B., and N. Sator (2007), A computer simulation study of natural silicate melts. Part II: High pressure properties, *Geochim. Cosmochim. Acta*, *71*, 4538–4556.
- Hernlund, J. W., and A. M. Jellinek (2010), Dynamics and structure of a stirred partially molten ultralow-velocity zone, *Earth Planet. Sci. Lett.*, *296*, 1–8.
- Hernlund, J. W., and P. J. Tackley (2007), Some dynamical consequences of partial melting in Earth's deep mantle, *Phys. Earth Planet. Inter.*, *162*, 149–163.
- Hier-Majumder, S. (2008), Influence of contiguity on seismic velocities of partially molten aggregates, *J. Geophys. Res.*, *113*, B12205, doi:10.1029/2008JB005662.
- Hier-Majumder, S. (2011), Development of anisotropic mobility during two-phase flow, *Geophys. J. Int.*, *186*, 59–68.
- Hier-Majumder, S., and M. E. Abbott (2010), Influence of dihedral angle on the seismic velocities in partially molten rocks, *Earth Planet. Sci. Lett.*, *299*, 23–32.
- Hier-Majumder, S., and A. Courtier (2011), Seismic signature of small melt fraction atop the transition zone, *Earth Planet. Sci. Lett.*, *308*, 334–342.
- Hier-Majumder, S., and J. Revenaugh (2010), Relationship between the viscosity and topography of the ultralow-velocity zone near the core-mantle boundary, *Earth Planet. Sci. Lett.*, *299*, 382–386.
- Hier-Majumder, S., P. Leo, and D. Kohlstedt (2004), On grain boundary wetting during deformation, *Acta Mater.*, *52*, 3425–3433.
- Hier-Majumder, S., Y. Ricard, and D. Bercovici (2006), Role of grain boundaries in magma migration and storage, *Earth Planet. Sci. Lett.*, *248*, 735–749.
- Hustoft, J., and D. Kohlstedt (2006), Metal silicate segregation in deforming dunitic rocks, *Geochem. Geophys. Geosyst.*, *7*, Q02001, doi:10.1029/2005GC001048.
- Hutko, A., T. Lay, and J. Revenaugh (2009), Localized double-array stacking analysis of PcP: D'' and ULVZ structure beneath the Cocos plate, Mexico, central Pacific and North Pacific, *Phys. Earth Planet. Inter.*, *173*, 60–74.
- Jellinek, A., and M. Manga (2004), Links between long-lived hotspots, mantle plumes, D'', and plate tectonics, *Rev. Geophys.*, *42*, RG3002, doi:10.1029/2003RG000144.
- King, D. S. H., S. Hier-Majumder, and D. L. Kohlstedt (2011), An experimental study of the effects of surface tension in homogenizing perturbations in melt fraction, *Earth Planet. Sci. Lett.*, *307*, 349–360.
- Leal, G. (1992), *Laminar Flow and Convective Transport Processes: Scaling Principles and Asymptotic Analysis*, 740 pp., Butterworth-Heinemann, Boston, Mass.
- Lissant, K. J. (1966), The geometry of high-internal-phase-ratio emulsions, *J. Colloid Interface Sci.*, *22*, 462–468.
- Manga, M., and H. Stone (1995), Low Reynolds number motion of bubbles, drops, and rigid spheres through fluid–fluid interfaces, *J. Colloid Interface Sci.*, *287*, 279–298.
- Mao, W. L., H.-K. Mao, W. Sturhahn, J. Zhao, V. B. Prakapenka, Y. Meng, J. Shu, Y. Fei, and R. J. Hemley (2006), Iron-rich post perovskite and the origin of the ultra low velocity zone, *Science*, *312*(5773), 564–565.
- Mavko, G., T. Mukerji, and J. Dvorkin (2003), *Rock Physics Handbook: Tools for Seismic Analysis of Porous Media*, 340 pp., Cambridge Univ. Press, Cambridge, U. K.
- McNamara, A. K., E. J. Garnero, and S. Rost (2010), Tracking deep mantle reservoirs with ultra-low velocity zones, *Earth Planet. Sci. Lett.*, *299*, 1–9.
- Mosenfelder, J. L., P. D. Asimow, and T. J. Ahrens (2007), Thermodynamic properties of Mg<sub>2</sub>SiO<sub>4</sub> liquid at ultra-high pressures from shock measurements to 200 GPa on forsterite and wadsleyite, *J. Geophys. Res.*, *112*, B06208, doi:10.1029/2006JB004364.

- Nomura, R., H. Ozawa, S. Tateno, K. Hirose, J. Hernlund, S. Muto, H. Ishii, and N. Hiraoka (2011), Spin crossover and iron-rich silicate melt in the Earth's deep mantle, *Nature*, *473*, 199–202.
- Ohtani, E., and M. Maeda (2001), Density of basaltic melt at high pressure and stability of the melt at the base of the lower mantle, *Earth Planet. Sci. Lett.*, *193*, 69–75.
- Ozawa, H., K. Hirose, M. Mitome, Y. Bando, N. Sata, and Y. Ohishi (2008), Chemical equilibrium between ferropericlase and molten iron to 134 GPa and implications for iron content at the bottom of the mantle, *Geophys. Res. Lett.*, *35*, L05308, doi:10.1029/2007GL032648.
- Ozawa, H., K. Hirose, M. Mitome, Y. Bando, N. Sata, and Y. Ohishi (2009), Experimental study of reaction between perovskite and molten iron to 146 GPa and implications for chemically distinct buoyant layer at the top of the core, *Phys. Chem. Miner.*, *36*, 355–363.
- Park, H. H., and D. K. Yoon (1985), Effect of dihedral angle on the morphology of grains in a matrix phase, *Metall. Trans. A*, *16*, 923–928.
- Poirier, J. P. (2000), *Introduction to the Physics of the Earth's Interior*, 2nd ed., 328 pp., Cambridge Univ. Press, Cambridge, U. K.
- Rost, S., and J. Revenaugh (2003), Small-scale ultralow-velocity zone structure imaged by *ScP*, *J. Geophys. Res.*, *108*(B1), 2056, doi:10.1029/2001JB001627.
- Rost, S., E. J. Garnero, Q. Williams, and M. Manga (2005), Seismological constraints on a possible plume root at the core-mantle boundary, *Nature*, *435*, 666–669.
- Rost, S., E. J. Garnero, and Q. Williams (2006), Fine-scale ultralow-velocity zone structure from high-frequency seismic array data, *J. Geophys. Res.*, *111*, B09310, doi:10.1029/2005JB004088.
- Scott, T., and D. Kohlstedt (2006), The effect of large melt fraction on the deformation behavior of peridotite, *Earth Planet. Sci. Lett.*, *246*, 177–187.
- Stixrude, L., and B. Karki (2005), Structure and freezing of MgSiO<sub>3</sub> liquid in Earth's lower mantle, *Science*, *310*(5746), 297–299.
- Stixrude, L., N. de Koker, N. Sun, M. Mookherjee, and B. B. Karki (2009), Thermodynamics of silicate liquids in the deep Earth, *Earth Planet. Sci. Lett.*, *278*, 226–232.
- Takei, Y. (1998), Constitutive mechanical relations of solid-liquid composites in terms of grain boundary contiguity, *J. Geophys. Res.*, *103*, 18,183–18,203, doi:10.1029/98JB01489.
- Takei, Y. (2000), Acoustic properties of partially molten media studied on a simple binary system with a controllable dihedral angle, *J. Geophys. Res.*, *105*, 16,665–16,682, doi:10.1029/2000JB900124.
- Takei, Y. (2002), Effect of pore geometry on  $V_P/V_S$ : From equilibrium geometry to crack, *J. Geophys. Res.*, *107*(B2), 2043, doi:10.1029/2001JB000522.
- Takei, Y. (2005), Deformation-induced grain boundary wetting and its effects on acoustic and rheological properties of partially molten rock analogue, *J. Geophys. Res.*, *110*, B12203, doi:10.1029/2005JB003801.
- Takei, Y., and S. Hier-Majumder (2009), A generalized formulation of interfacial tension driven fluid migration with dissolution/precipitation, *Earth Planet. Sci. Lett.*, *288*, 138–148.
- ten Grotenhuis, S., M. Drury, C. Spiers, and C. J. Peach (2005), Melt distribution in olivine rocks based on electrical conductivity experiments, *J. Geophys. Res.*, *110*, B12201, doi:10.1029/2004JB003462.
- Thorne, M., and E. Garnero (2004), Inferences on ultralow-velocity zone structure from a global analysis of *SPdKS* waves, *J. Geophys. Res.*, *109*, B08301, doi:10.1029/2004JB003010.
- von Bargen, N., and H. Waff (1986), Permeabilities, interfacial areas, and curvatures of partially molten systems: Results of numerical computations of equilibrium microstructures, *J. Geophys. Res.*, *91*, 9261–9276.
- Walsh, J. (1969), New analysis of attenuation in partially molten rocks, *J. Geophys. Res.*, *74*, 4333–4337, doi:10.1029/JB074i017p04333.
- Wang, Y., and L. Wen (2004), Mapping the geometry and geographic distribution of a very low velocity province at the base of the Earth's mantle, *J. Geophys. Res.*, *109*, B10305, doi:10.1029/2003JB002674.
- Wark, D., and E. Watson (2000), Effect of grain size on the distribution and transport of deep-seated fluids and melts, *Geophys. Res. Lett.*, *27*, 2029–2032.
- Watson, H. C., and J. J. Roberts (2011), Connectivity of core forming melts: Experimental constraints from electrical conductivity and X-ray tomography, *Phys. Earth Planet. Inter.*, *186*, 172–182.
- Watt, J. P., G. F. Davies, and R. J. O'Connell (1976), The elastic properties of composite materials, *Rev. Geophys.*, *14*, 541–563, doi:10.1029/RG014i004p00541.
- Wen, L. (2001), Seismic evidence for a rapidly varying compositional anomaly at the base of the Earth's mantle beneath the Indian Ocean, *Earth Planet. Sci. Lett.*, *194*, 83–95.
- Wen, L. (2006), A compositional anomaly at the Earth's core-mantle boundary as an anchor to the relatively slowly moving surface hotspots and as source to the DUPAL anomaly, *Earth Planet. Sci. Lett.*, *246*, 138–148.
- Wen, L., and D. Helmberger (1998), Ultra-low velocity zones near the core-mantle boundary from broadband PKP precursors, *Science*, *279*(5357), 1701–1703.
- Wen, L., P. Silver, D. James, and R. Kuehnel (2001), Seismic evidence for a thermo-chemical boundary at the base of the Earth's mantle, *Earth Planet. Sci. Lett.*, *189*, 141–153.
- Wicks, J. K., J. M. Jackson, and W. Sturhahn (2010), Very low sound velocities in iron-rich (Mg,Fe)O: Implications for the core-mantle boundary region, *Geophys. Res. Lett.*, *37*, L15304, doi:10.1029/2010GL043689.
- Williams, Q., and E. Garnero (1996), Seismic evidence for partial melt at the base of Earth's mantle, *Science*, *273*(5281), 1528–1530.
- Wimert, J. (2011), A semianalytical, three-dimensional model of microstructure in multiparticle, multiphase flow, master's thesis, Univ. of Md., College Park.
- Yoshino, T., Y. Takei, D. Wark, and E. Watson (2005), Grain boundary wetness of texturally equilibrated rocks, with implications for seismic properties of the upper mantle, *J. Geophys. Res.*, *110*, B08205, doi:10.1029/2004JB003544.
- Zhu, W., and G. Hirth (2003), A network model for permeability in partially molten rocks, *Earth Planet. Sci. Lett.*, *212*, 407–416.
- Zhu, W., G. Gaetani, F. Fusses, L. Montési, and F. De Carlo (2011), Microtomography of partially molten rocks: Three-dimensional melt distribution in mantle peridotite, *Science*, *332*(6025), 88–91.

S. Hier-Majumder and J. Wimert, Department of Geology, University of Maryland, College Park, MD 20742, USA. (saswata@umd.edu)